

PARTICLE ACCELERATION AND NON-THERMAL EMISSION IN PULSAR OUTER MAGNETOSPHERIC GAP

J. Takata,^{1?}, H.-K. Chang², and S. Shibata³

¹Institute of Astronomy and Astrophysics, and Theoretical Institute for Advanced Research in Astrophysics, Academia Sinica; and National Tsing Hua University

²Department of Physics and Institute of Astronomy, National Tsing Hua University, Hsinchu, Taiwan

³Department of Physics, Yamagata University, Yamagata, Japan

ABSTRACT

A two-dimensional electrodynamic model is used to study particle acceleration and non-thermal emission mechanisms in the pulsar magnetospheres. We solve the distribution of the accelerating electric field with the emission process and the pair-creation process in the meridional plane, which includes the rotational axis and the magnetic axis. By solving the evolutions of the Lorentz factor, and of the pitch angle, we calculate the spectrum in optical through γ -ray bands with the curvature radiation, synchrotron radiation, and inverse-Compton process not only for outgoing particles, but also for ingoing particles, which were ignored in previous studies.

We apply the theory to the Vela pulsar. We find that the curvature radiation from the outgoing particles is the major emission process above 10 MeV bands. In soft γ -ray to hard X-ray bands, the synchrotron radiation from the ingoing primary particles in the gap dominates in the spectrum. Below hard X-ray bands, the synchrotron emissions from both outgoing and ingoing particles contribute to the calculated spectrum. The calculated spectrum is consistent with the observed phase-averaged spectrum of the Vela pulsar.

Taking into account the predicted dependency of the emission process and the emitting particles on the energy bands, we compute the expected pulse profile in X-ray and γ -ray bands with a three-dimensional geometrical model. We show that the observed γ -peak pulse profile in the X-ray bands of the Vela pulsar is reproduced by the inward and outward emissions, and the

observed double-peak pulse profile in γ -ray bands is explained by the outward emissions.

We also apply the theory to PSR B1706-44 and PSR B1951+32, for which X-ray emission properties have not been constrained observationally very well, to predict the spectral features with the present outer gap model.

Key words: pulsars: general { radiation mechanism: non-thermal

1 INTRODUCTION

The Compton Gamma-Ray Observatory (CGRO) had measured pulsed γ -ray emissions from younger pulsars (Thompson 2004). The multi-wavelength observations of the γ -ray pulsars have shown that the spectra of the non-thermal emissions extend in γ -ray through optical bands. The observations have also revealed the pulse profiles in optical through γ -ray bands, and the polarization properties of the pulsed optical emissions from the γ -ray pulsars (Kanbach et al. 2005; Mignani et al. 2007). In the future, furthermore, the polarization of the X-rays and γ -rays from the pulsars will probably be able to be measured by ongoing projects (Kamae et al. 2007; Chang et al. 2007). The multi-wavelength observations on the spectrum, the pulse profile and the polarization allow us to perform a comprehensive theoretical discussion for the mechanisms of the particle acceleration and of the non-thermal emission in the pulsar magnetospheres.

The particle acceleration and the non-thermal emission processes in the pulsar magnetosphere have been mainly argued with the polar cap accelerator model (Sturrock 1971; Ruderman & Sutherland 1975) and the outer gap accelerator model (Cheng, Ho & Ruderman 1986a, 1986b). Also, the slot gap model (Muslinov and Harding 2004), which is an extension model of the polar cap model, was proposed. All models predict an acceleration of the particles by an electric field parallel to the magnetic field. In the pulsar magnetosphere, the accelerating electric field arises in a charge depletion region from the so called Goldreich-Julian charge density (Goldreich & Julian 1969), and the strong acceleration region in the magnetosphere depends on the model. The polar cap and the slot gap models predict a strong acceleration within several stellar radii on the polar cap, and the outer gap model predicts a strong acceleration beyond the null charge surface, on which the Goldreich-Julian charge density becomes zero.

As CGRO had observed, most of the γ -ray pulsars have a double peak structure in the pulse profile in γ -ray bands. The outer gap model has been successful in explaining the observed double peak structure (Romani & Yadigaroglu 1995). With the outer gap model, the double peak structure is naturally produced as an effect of the aberration and the time delay of the emitted photons by the outgoing particles that move toward the light cylinder, which is defined by the positions, on which the rotating speed with the star is equal to speed of the light. The axial distance of the light cylinder is $R_{lc} = c/\Omega$, where c is the speed of the light, and Ω is the angular velocity of the neutron star.

Because the Crab pulsar has the pulse profiles with the double peak structure in whole energy bands, the outer gap model can explain the pulse profiles of the Crab pulsar in optical through γ -ray bands (Takata & Chang 2007). Furthermore, the outer gap model can explain the observed spectra, and the polarization characteristics in optical bands for the Crab pulsar (Cheng et al. 2000; Hirokuni 2007; Jia, et al 2007; Takata et al, 2007; Takata & Chang 2007; Tang et al. 2007). Therefore, the outer gap accelerator model has successfully explained the results of the multi-wave length observations for the Crab pulsar.

For the Vela pulsar, multi-peak structure in pulse profiles in X-ray, UV and optical bands have been revealed (Harding et al. 2002; Romani et al. 2005), although the pulse profile in γ -ray bands has two peaks in a single period (Fierro et al. 1998). For example, Harding et al. (2002) analysed RXTE data and revealed the pulse profile, which has at least five peaks in a single period. Because the two peaks in the five peaks are in phase with the two peaks in the γ -ray bands, the two peaks will be explained by the traditional outer gap model with the outward emissions from the outer gap. However, because other three peaks are not expected by the traditional outer gap model, the origin of the three peaks has not been understood, so far.

The inward emissions emitted by particles accelerated toward stellar surface will give one possibility to explain the unexpected three peaks of pulse profile in the X-ray bands of the Vela pulsar. Because the primary particles are produced near the inner boundary of the gap, the ingoing particles feel a small part of whole potential drop in the gap before escaping the gap from the inner boundary, although the outward moving particles can feel whole potential drop before escaping the gap from the outer boundary. In previous studies, therefore, the contribution of the inward emissions on the spectral calculation has been ignored by assuming that its flux is much smaller than that of the outward emissions. However, it will be true only in the γ -ray bands with the curvature radiation. Because

main emission mechanism in the X-ray bands will be the synchrotron radiation, the inward synchrotron emissions with a stronger magnetic field will be efficient enough to contribute on the observed emissions below γ -ray bands. Although the inward emissions have been consistently dealt in the electrodynamic studies (Takata et al. 2006; Hirokani, 2007), only the outward emissions were taken into account for computing the spectrum.

In this paper, we calculate the spectrum in optical through γ -ray bands by taking into account both inward and outward emissions. Specifically, we solve the electrodynamics in the outer gap accelerator in the two-dimensional plane, which includes the rotational axis and the magnetic axis. We calculate the spectrum of the curvature radiation, synchrotron radiation, and inverse Compton process for the primary and the secondary particles. We also discuss the expected pulse profiles from optical through γ -ray bands with a three-dimensional model for comparison with the observations. Furthermore, we apply the theory to PSRs B 1706-44 and B 1951+32 to calculate the spectrum, because the properties of optical and X-ray emissions from the two pulsars have not been understood well.

In section 2, we describe our two-dimensional electrodynamic model following Takata et al. (2004, 2006). In section 3, we apply the theory to the Vela pulsar, and we discuss the spectrum and the pulse profile in optical through γ -ray bands. We also show the expected spectra of PSRs B 1706-44 and B 1951+32.

2 TWO-DIMENSIONAL ELECTRODYNAMIC MODEL

We consider a stationary structure in the meridional plane, which includes the magnetic axis and the rotation axis. In the meridional plane, we solve the Poisson equation of the accelerating electric field, the continuity equations for electron and for positron on each magnetic field line, and the pair-creation process by γ -ray and the surface X-rays (section 2.1). We assume that new born particles via pair-creation process in the gap is quickly saturated between the accelerating force and the curvature radiation back reaction force, instead solving the evolutions of the Lorentz factor and of the pitch angle of the particles. To obtain the electric structure, the saturation treatment is a good assumption, and simplifies the problem to obtain a outer gap structure with an iterating method (section 2.2).

In the method described above, however, we can not calculate the synchrotron radiation of the new born pairs because we do not solve the pitch angle evolution, although the synchrotron radiation is an important emission mechanism in the X-ray regions. With obtained

electric structure with our dynamic model, therefore, we solve the evolutions of the Lorentz factor and of the pitch angle of the particles for calculating the synchrotron radiation process in the gap (section 2.3). In this paper, we take into account the curvature radiation, the synchrotron radiation, and the inverse-Compton processes (section 2.4). We consider the magnetized rotator that an inclination angle between the rotation axis and the magnetic axis is smaller than 90° . We use a dipole magnetic field to solve the structure of the outer gap.

2.1 Stationary gap structure

The stationary electric potential, ϕ_{∞} , for the accelerating field is obtained from (Mestel 1999)

$$\nabla^2 \phi_{\infty}(r) = -4 [\rho(r) - \rho_{GJ}(r)]; \quad (1)$$

where $\rho(r)$ is the space charge density, and $\rho_{GJ}(r)$ is the Goldreich-Julian charge density (Goldreich & Julian 1969), $\rho_{GJ} = B_z/2c$. We assume that the gap dimension in the azimuthal direction is much larger than that in the meridional plane. Neglecting variation in the azimuthal direction, we rewrite equation (1) as

$$\nabla_r^2 \phi_{\infty}(r) = -4 [\rho(r) - \rho_{GJ}(r)]; \quad (2)$$

where ∇_r^2 represents $(r;)$ -parts of the Laplacian.

The continuity equations for the particles is written as

$$B \frac{v_{\parallel}}{r} \frac{dN_{\pm}(r)}{dr} = S(r); \quad (3)$$

where $v_{\parallel} < c$ is the velocity along the field line, $S(r)$ is the source term due to the pair-creation process, and N_+ and N_- denote the number density of the outgoing and ingoing particles (i.e. the positrons and electrons in the present case), respectively. In the outer gap accelerator, $\gamma + X \rightarrow e^+ + e^-$ process is the main pair-creation process, and contributes to the source term $S(r)$ in equation (3). The pair-creation rate is calculated from

$$\dot{N}_p(r; E) = (1 - \cos \chi) c \int_{E_{th}}^{\infty} dE_X \frac{dN_X}{dE_X}(r; E_X) \dot{N}_p(E; E_X);$$

where dN_X/dE_X is the X-ray number density between energies E_X and $E_X + dE_X$, χ is the collision angle between an X-ray photon and a γ -ray photon, $E_{th} = 2(m_e c^2)^2/(1 - \cos \chi)E$ is the threshold X-ray energy for the pair creation, and \dot{N}_p is the pair creation cross-section, which is given by

$$P(E_{\gamma}; E_X) = \frac{3}{16} \sigma_T (1 - \beta^2) (3 - \beta^2) \ln \frac{1 + \beta}{1 - \beta} - 2\beta (2 - \beta^2); \quad (4)$$

where

$$\beta(E_{\gamma}; E_X) = \frac{v}{c} \frac{1}{1 + \frac{2}{1 - \cos \theta} \frac{(m_e c^2)^2}{E E_X}};$$

and σ_T is the Thomson cross section. In the gap, the GeV photons collide with the thermal X-ray photons from the stellar surface. At the radial distance r from the centre of the star, the thermal photon number density between energy E_X and $E_X + dE_X$ is given by

$$\frac{dN_X}{dE_X} = 2 \frac{1}{ch} \frac{R_{\text{eff}}^2}{r} \frac{E_X^2}{\exp(E_X/kT_s) + 1}; \quad (5)$$

where R_{eff} is the effective radius of the emitting region, and kT_s refers to the surface temperature. For the values of R_{eff} and T_s , the observed ones are used. Because the γ -ray photons are emitted in direction of velocity of the particles, the collision angle is estimated from $\cos \theta = v_{\text{ej}} B_r / cB$, where B_r is the radial component of the magnetic field.

To calculate the source term $S(r)$ in equation (2) at each point, we simulate the photon-photon pair-creation process with Monte Carlo method as described in Takata et al (2006). Specifically, a γ -ray may convert into a pair at the distance s with the probability that

$$P_p(s) = \frac{\int_0^{R_s} 1 - \exp(-s/l_p) ds}{l_p}; \quad (6)$$

where $l_p = c/\sigma_p$ is the mean-free path of the pair-creation. We determine the pair-creation position following the probability of equation (6).

Most of GeV photons are emitted via the curvature process of the electrons and the positrons with the Lorentz factor of $\sim 10^{7.5}$. The power per unit energy of the curvature process is written as

$$P_c(R_c; E) = \frac{P}{3e^2} \frac{1}{hR_c} F(x); \quad (7)$$

where $x = E/E_c$,

$$E_c = \frac{3}{4} \frac{hc^3}{R_c}; \quad (8)$$

and

$$F(x) = x \int_x^{Z_1} K_{5/3}(t) dt; \quad (9)$$

where R_c is the curvature radius of the magnetic field line, γ is the Lorentz factor of the particles, $K_{5/3}$ is the modified Bessel function of the order 5/3, h is the Planck constant, and E_c gives the characteristic curvature photon energy.

We assume the saturated motion to obtain the stationary electric field structure. By assuming that the particle's motion immediately saturates in the balance between the electric and the radiation reaction forces, the Lorentz factor at each point is calculated from

$$\gamma_{\text{sat}}(R_c; E_{\text{eff}}) = \frac{3R_c^2 E_{\text{eff}}^2}{2e} + 1 \quad (10)$$

2.2 Boundary conditions

To solve the Poisson equation (2), we impose the boundary conditions on the four boundaries, which are called as inner, outer, upper and lower boundaries. The lower and upper boundaries are laid on the magnetic surfaces, and the lower boundary is defined by the last open field line. The inner and the outer boundaries are defined by the surfaces on which the accelerating electric field is vanishes, that is, $E_{\text{eff}} = 0$.

We anticipate that the inner, upper, and lower boundaries are directly linked with the star without the potential drop. We then impose that the accelerating potential is equal to zero, that is $\phi = 0$, on the inner, upper and lower boundaries. We note that the position of the inner boundary is not free because the Dirichlet- and Neumann-type conditions are imposed on it. By moving the inner boundary step by step iteratively, we seek the boundary that satisfies the required conditions.

As demonstrated in Takata et al. (2004), the inner boundary, which is satisfied the required conditions, comes to the position, on which the condition that $j_y + j_z = B_z = B$ is satisfied, where j_y is the current in units of the Goldreich-Julian value carried by the pairs produced in the gap, j_z is the current carried by the positrons coming into the gap through the inner boundary and j_x is the current carried by the electrons coming into the gap through the outer boundary. We find that if there is a current in the outer gap, the inner boundary is shifted from the null charge surface, where is the inner boundary for the vacuum gap, $j_y = j_z = j_x = 0$. Total current in unit of the Goldreich-Julian charge density is described by $j_{\text{tot}} = j_y + j_z + j_x$ and is constant along a field line. The model parameters are the current $(j_z; j_x; j_y)$ and the inclination angle α . A more detail discussion on the boundary conditions and the model parameters is seen in Takata et al. (2004, 2006).

2.3 Particle motion

To compute the synchrotron radiation with the pitch angle, we use the electric field distribution in the outer gap obtained by the method described in section 2.1 to solve the equation of

motion, which describes the evolutions of the pitch angle of the particle. For the Vela pulsar, the inverse-Compton process is less significant for energy loss of the particles than the synchrotron and curvature radiation. The momenta of the parallel ($P_{\parallel} = \gamma m_e c = \frac{p}{\gamma} \cos \theta_p$) and perpendicular ($P_{\perp} = \gamma m_e c = \frac{p}{\gamma} \sin \theta_p$) to the magnetic field are, respectively, described as (Harding et al. 2005; Hirokuni 2006)

$$\frac{dP_{\parallel}}{dt} = eE_{\parallel} - P_{sc} \cos \theta_p; \quad (11)$$

and

$$\frac{dP_{\perp}}{dt} = -P_{sc} \sin \theta_p + \frac{c}{2B} \frac{dB}{ds} P_{\perp}; \quad (12)$$

where θ_p is the pitch angle, P_{sc} represents the radiation drag of the synchrotron and curvature radiation, and the second term on the right hand side on equation (12) represents the adiabatic change along the dipole field line. The radiation drag, P_{sc} , of the synchrotron-curvature radiation is described by (Cheng & Zhang 1996),

$$P_{sc} = \frac{e^2 c^4 Q_2}{12 r_c} \left(1 + \frac{7}{r_c^2 Q_2^2} \right); \quad (13)$$

where

$$r_c = \frac{c^2}{(r_B + R_c) (c \cos \theta_p = R_c)^2 + r_B^2}; \quad (14)$$

$$Q_2^2 = \frac{1}{r_B} \left(\frac{r_B^2 + R_c r_B}{R_c^3} \cos^4 \theta_p + \frac{3}{R_c} \cos^2 \theta_p + \frac{1}{r_B} \sin^4 \theta_p \right); \quad (15)$$

$$r_B = \frac{m_e c^2 \sin \theta_p}{eB}; \quad \gamma_B = \frac{eB}{m_e c}; \quad (16)$$

We solve the equations of the motion, (11) and (12), up to the light cylinder for the outgoing particles (positrons) and to the stellar surface for the ingoing particles (electrons). The initial pitch angle of the newborn pairs is determined by the angle between the propagating direction of γ -rays and the direction of the magnetic field at the pair-creation point.

2.4 Spectra of radiation processes

We calculate the curvature radiation, synchrotron radiation and inverse-Compton process. The power of the synchrotron-curvature process for a particle is calculated from (Cheng & Zhang 1996),

$$\frac{dP}{dE} = \frac{p}{4 r_c E_c} \left(\frac{E}{E_c} \right)^{Z-1} K_{5/2} \left(\frac{E}{E_c} \right) + \frac{[(r_B + R_c) (c \cos \theta_p = R_c)^2 + r_B^2]}{c^4 Q_2^2} \left(\frac{E}{E_c} \right)^{Z-1} K_{5/2} \left(\frac{E}{E_c} \right) + K_{2/3} \left(\frac{E}{E_c} \right); \quad (17)$$

Very high-energy γ -rays are produced by the inverse Compton process. The emissivity of the inverse Compton process for a particle is calculated from (Takata & Chang 2007)

$$\frac{dP_{in}}{dE d\Omega} = D^2 \int_0^{\pi/2} (1 - \cos \theta_0) I_b d\Omega_0; \quad (18)$$

where θ_0 is the angle between the directions of the particle motion and the propagating direction of the background photon, $D = \frac{1}{(1 - \cos \theta_1)^{1/2}}$ with θ_1 being the angle between the directions of the particle motion and the propagating direction of the scattered photons. The angle $\theta_c = \sin^{-1} R/r$, with R being stellar surface, expresses the size of the star seen from the point r , $d\Omega_0$ is the solid angle of the background radiation. The differential cross section is given by the Klein-Nishina formula

$$\frac{d\sigma_0}{d\Omega_0} = \frac{3}{16} \frac{\tau_0}{\gamma_0^2} \left[\frac{\gamma_0}{\gamma_1} + \frac{\gamma_1}{\gamma_0} \right] \sin^2 \theta_0; \quad (19)$$

where γ_0 and γ_1 are the energy of the background and the scattered photons in units of the electron rest mass energy, respectively, in the electron rest frame, and they are connected each other by $\gamma_1 = \gamma_0 [1 + \gamma_0 (1 - \cos \theta_s^0)]$. The scattering angle θ_s^0 is defined by

$$\cos \theta_s^0 = \sin \theta_0 \sin \theta_1 \cos(\phi_0 - \phi_1) + \cos \theta_0 \cos \theta_1 \quad (20)$$

where θ_0 and θ_1 are the polar angle of the propagating direction of the background and the scattered photons, respectively, measured from the particle motion in the electron rest frame, ϕ_0 and ϕ_1 are the azimuthal directions of the photons.

In the present model, we adopt the surface thermal emission as the background field of the inverse Compton process. In such a case, the intensity I_b is described by the Planck distribution that

$$I_b(E_X) = \frac{2E_X^3 / h^2 c^2}{\exp(E_X / kT_s) - 1}; \quad (21)$$

We calculate the emissions from the following four different kind of electron and positron,

- (i) primary particles, which are created inside the gap, and are accelerated up to ultra-relativistic energy;
- (ii) secondary particles created outside the gap via the photon-photon pair-creation process by the surface thermal X-ray photons;
- (iii) secondary particles created outside the gap via the photon-photon pair-creation process by the magnetospheric non-thermal X-ray photons;
- (iv) secondary particles created outside the gap via the magnetic pair-creation.

For the magnetic pair-creation, we assume that γ -ray photons are converted into the pairs

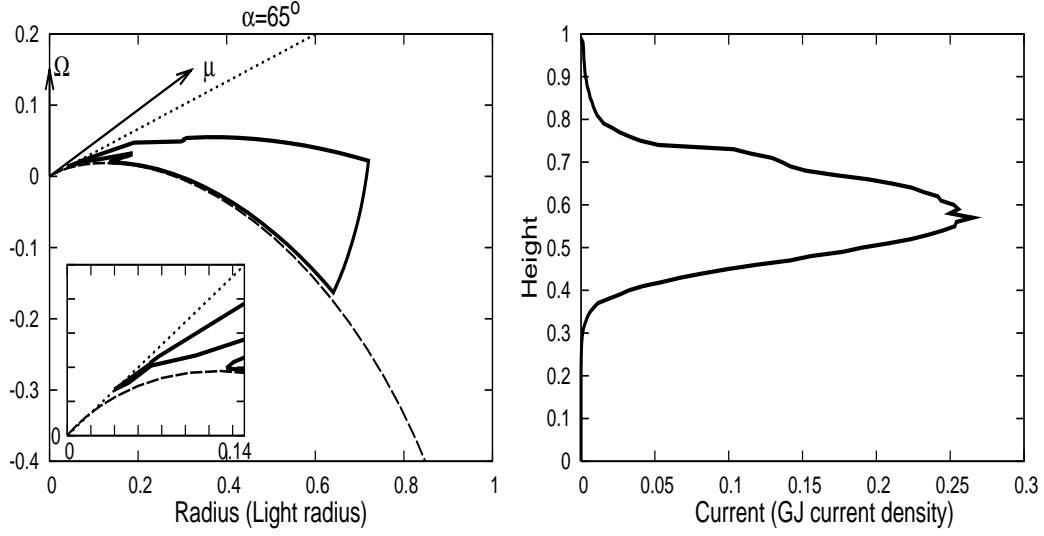


Figure 1. Left; The geometry of the outer gap accelerator. The solid line is the boundary of the gap. The dashed line shows the last-open line. For the dotted line, the condition that $B_z = 0.26 B$ is satisfied. Right; The transverse structure of the current. The inclination angle is $\alpha = 65^\circ$.

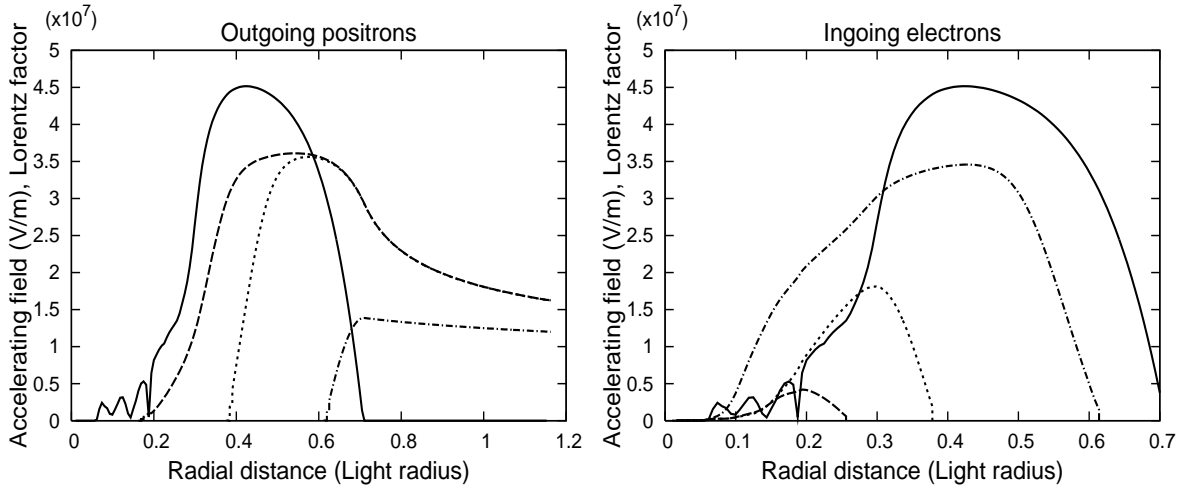


Figure 2. Evolution of the Lorentz factor of the outgoing positrons (the left panel) and the ingoing electrons (the right panel) along a magnetic field line. The dashed, dotted and dashed-dotted lines are for the particles produced near the inner boundary, produced in the middle of the gap and produced near the outer boundary, respectively. The solid lines show the distribution of the accelerating electric field along the field line.

at the point, on which the condition that $E \cdot B \sin \theta_p = B_{cr} = 0.2 m_e c^2$ (Muslinov & Harding 2003) is satisfied, where $B_{cr} = 4.4 \times 10^{13}$ Gauss is the strength of the critical magnetic field. The TeV photons emitted by the inverse-Compton process also produce the secondary pairs. Because the flux of the TeV radiation is much smaller than the flux of GeV radiation (Figure 3), we ignore the emissions for the pairs produced by the TeV photons.

3 RESULTS

3.1 The Vela pulsar

In this section, we apply the theory to the Vela pulsar. With the outer gap model, Romani & Yadigaroglu (1995) used $\alpha = 65^\circ$ to produce the pulse profile of the γ -ray emissions from the Vela pulsar. This inclination angle will be consistent with the inclination angle $\alpha = 60^\circ$ for fitting the polarization swing of the radio emissions (Krishnamohan & Downs 1983). In this paper, we adopt $\alpha = 65^\circ$ to the Vela pulsar. For the thermal emissions from the stellar surface, we use the temperature $kT_s = 0.1$ keV with the effective radius $R_{\text{eff}} = 4.4(d=0.25 \text{ kpc})^2 \text{ km}$ (Manzali et al. 2007). We assume a small injection of the particles through the boundaries with $j_1 = 10^{-5}$ and $j_2 = 0$. In such a case, the total current is carried by the pairs created inside the gap, that is, $j_{\text{tot}} = j_{\text{gap}}$. In this paper, we show the outer gap structure that extends from near the stellar surface.

3.1.1 Outer-gap structure

Figure 1 summarises the outer gap geometry in the magnetosphere and the current in the gap. Figure 1 (the thick solid line in the left panel) shows the boundary of the outer gap. Inside of the thick solid line, the particles are accelerated along the magnetic field lines. The dashed line in the figure shows the last open field line. The trans-field distribution of the current is shown in Figure 1 (right). The abscissa refers the current in unit of the Goldreich-Julian value, $B = 2$, and the vertical line represents the height measured from the last open field line. For example, we can read from the figure that about 26% of the Goldreich-Julian current runs through the gap at the height of the 60% of the thickness measured from the last open field line.

As discussed in Takata et al. (2004, 2006), the inner boundary with a small particle injections is located at the position, on which $B_z = j_y B$ is satisfied. For example, if $j_y = 0$, that is, if the gap is vacuum, the inner boundary comes to the position, on which $B_z = 0$, and therefore the null charge surface becomes the inner boundary of the gap. If there is the pair-creation in the gap, on the other hand, the inner boundary is shifted toward the stellar surface due to the current.

The sub-panel in the left panel of Figure 1 zooms the region around the inner boundary. The dotted line in the figure shows the position, on which the condition $B_z = 0.26B$, where $j_y = 0.26$ is the maximum current in the outer gap, is satisfied. We can see that the cusp of

the inner boundary, where the maximum current runs through on the field line, is located on the dotted line. Thus, the outer gap can extend near the stellar surface with a large current.

3.1.2 Particle motion

Figure 2 summarizes the distribution of the accelerating electric field and the evolutions of the accelerated particles along the field line, which penetrates the outer gap at the height of 50% of thickness. The left and the right panels show the evolutions of the Lorentz factors of the outgoing and ingoing particles, respectively, and represent for the three kinds of the particles, which are produced near the inner boundary (the dashed line), middle of the gap (the dotted line) and near the outer boundary (the dashed-dotted line). The solid lines in the figure show the distribution of the strength of the accelerating electric field along the field line.

For example, a positron produced middle point of the gap (Figure 2, the dotted line in the left panel) is outwardly accelerated by the electric field, and is immediately boosted above 10^7 on the Lorentz factor. This positron escapes from the outer gap around $r = 0.7$, where the accelerating field vanishes. Because there is no accelerating electric field outside the gap, the particles lose their energy via the curvature radiation. Because the cooling length of the curvature radiation, $l_{\text{cool}} = R_{\text{LC}} \approx 1.6 (R_c = R_{\text{LC}})^2 (\gamma = 10^7)^{-3} (\omega = 100 \text{ s}^{-1})^{-1}$, becomes comparable with the light radius at the Lorentz factor of 10^7 , the particles escape from the light cylinder with the Lorentz factor of 10^7 . If the particle was not accelerated above 10^7 inside the gap such as the positrons produced near the outer boundary (Figure 2, the dashed-dotted line in the left panel), the Lorentz factor of the particles does not change very much between the outer boundary and the light cylinder.

An electron produced middle of the gap (Figure 2, the dotted line in the right panel) is inwardly accelerated by the electric field, and are also immediately boosted above 10^7 on the Lorentz factor in the gap. The accelerated electrons significantly lose their energy near and outside the inner boundary due to the curvature radiation. This is because the curvature radius near the stellar surface is about $R_c \approx 10^7 \text{ cm}$, and therefore the radiation drag force near the stellar surface is strong so that the cooling length is much shorter than light radius, if the Lorentz factor is larger 10^7 . The primary electrons reach the stellar surface with the Lorentz factor of 10^6 .

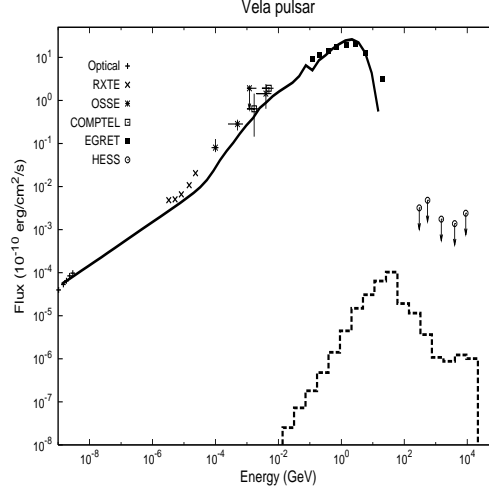


Figure 3. Spectrum of the Vela pulsar. The solid line shows the total spectrum of the curvature and the synchrotron radiation from the primary and the secondary particles. The dashed line shows the spectrum of the inverse-Compton process of the primary particles. The observation data are taken from Shibano et al. (2003) for optical, Harding et al. (2002) for RXTE, Strickman et al. (1996) for OSSE and COMPTEL, Fierro et al. (1999) for EGRET and Konopelko et al. (2005) for HESS.

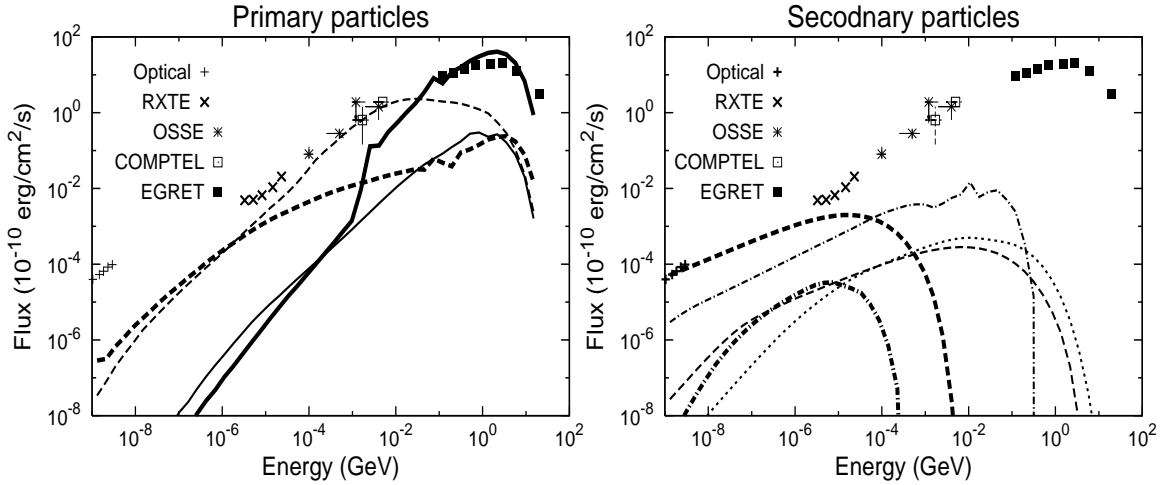


Figure 4. Spectrum of the Vela pulsar. Left; Spectra of the curvature (the solid lines) and synchrotron (the dashed lines) radiation from the primary particles. The thick and thin lines show the emissions from the outgoing particles and ingoing particles, respectively. Right; Spectra of the synchrotron radiation of the secondary particles. The dashed line shows the synchrotron spectra of the pairs produced by the pair-creation process by the magnetospheric X-rays. The dashed-dotted lines are the spectra of the pairs produced by the pair-creation process with surface thermal X-rays. The dotted line shows the spectra of the secondary pairs produced via the pair-creation process with the strong magnetic field. The thick and thin lines show the emissions from the outgoing particles and ingoing particles, respectively.

3.1.3 Spectrum

Figure 3 shows the calculated spectrum from the optical through TeV bands. Figure 3 (the solid line) shows the spectrum of the total emissions, which include the curvature and the synchrotron radiation from the primary and the secondary particles. The dashed line is the inverse-Compton spectrum of the primary particles. The observational data of the phase-

averaged spectrum are also plotted. We find that the calculated spectrum is consistent with the observations in whole energy bands.

In Figure 4, we decompose the total spectrum (Figure 3, the solid line) into the components of the primary particles (the left panel) and of the secondary particles (the right panel). In the left panel, the solid lines and the dashed line show the spectra of the curvature radiation and the synchrotron radiation of the primary particles, respectively. The thick line and the thin line represent the spectra of the outward emissions for the outgoing positrons and of the inward emissions for the ingoing electrons, respectively.

For the outward emissions of the primary particles, we can see that the ratio of the radiation powers of the curvature radiation P_c (Figure 4, the thick solid line in the left panel) and the synchrotron radiation P_s (Figure 4, the thick dashed line in the left panel) is about $P_c/P_s \approx 10^3$. The perpendicular momentum to the magnetic field lines quickly decreases via the synchrotron radiation, and its cooling length is much shorter than the gap width. Therefore the synchrotron radiation from the primary particles are efficient only near the pair-creation position, which is around the inner boundary of the gap. On the other hand, the outward curvature radiation of the outgoing particles takes place at whole outer gap, because the particles are always accelerated by the electric field in the gap. In such a case, the ratio of the total powers is estimated with $P_c/P_s \approx (2e^4 s/R_c^2)/m^2 c^2 \gamma^3 \Omega^4 (\gamma=10^3)^{-1} (s=0.5R_{lc})$, where s is the gap width. This estimated value P_c/P_s explains the ratio between the calculated fluxes of the outward curvature emissions and of the synchrotron emissions. Although the total power of the outward synchrotron radiation is smaller than that of the curvature radiation, the emissions become important below 1 MeV bands as Figure 4 (the thick dashed line in the left panel) shows.

For ingoing primary electrons (Figure 4, the thin lines in the left panel), the travel distance in the gap before escaping from the inner boundary is much shorter than the gap width, because the most pairs are produced near the inner boundary. And, because the maximum Lorentz factor of the ingoing electrons is $\approx 10^7$, which is smaller than that of the outgoing positrons, the ratio of the radiation powers P_c/P_s becomes about unity as Figure 4 (the thin solid and dashed lines in the left panel) shows.

With Figure 4 (the right panel), we show the spectra of the synchrotron emissions for three kinds of the secondary pairs; the dashed lines show the spectra for the secondary pairs produced by the magnetospheric X-rays, the dashed-dotted lines represent the spectra for the pairs produced by the surface X-rays, and the dotted line shows the spectrum for

the pairs produced via the magnetic pair-creation process. The thick and thin dashed lines represent the synchrotron spectra from the outgoing and ingoing moving pairs, respectively.

As Figure 4 (the dashed-dotted lines) shows, the synchrotron emissions from the outgoing pairs produced by the surface X-rays are much fainter than that from the ingoing particles. For the outwardly propagating γ -rays, the pair-creation process by the surface X-ray occurs with tail-on-like collision, that is, $1 - \cos \chi \approx 1$. For the ingoing propagating γ -rays, on the other hand, the pair-creation process by the surface X-ray occurs with head-on-like collision, that is, $1 - \cos \chi \approx 2$. This difference of the collision angle produces a large difference in the mean free path so that the mean-free path of the outgoing γ -rays is much longer than that of the ingoing γ -rays. Because a smaller number of the outgoing secondary pairs than that of the ingoing secondary pairs are produced by the surface X-rays, the flux of the synchrotron emissions for the outgoing pairs is much fainter than that for the ingoing pairs.

For the secondary pairs produced by the magnetospheric X-ray photons, on the other hand, the total energy of synchrotron emissions for the outgoing particles is much larger than that for the ingoing particles (Figure 4, the dashed lines in the right panel). Because the collision angles with the magnetospheric X-ray are not different between the outer outgoing and ingoing γ -ray photons, the difference of number of the created pairs originates from the difference of the number of the γ -ray photons. Because the outgoing γ -rays are more than that the ingoing γ -rays as Figure 4 (the left panel) shows, more outgoing secondary pairs are produced than the ingoing secondary pairs. Therefore, the synchrotron emissions for the outgoing secondary pairs produced by the magnetospheric X-rays are brighter than that for the ingoing secondary pairs. This will be the main reason of the fact that the Crab pulsar has the double peak pulse profile structure in whole energy bands (section 4.3).

Using Figure 4, we know which emission process is important in the spectrum in different energy bands. Above 10 MeV, we see that the curvature radiation of the outgoing primary particles (Figure 4, the thick solid line in the left panel) dominates other emission processes, and explains the EGRET observations, as previous studies discussed (Romani 1996; Takata et al. 2006). We find that between 100 keV and 10 MeV bands, the synchrotron radiation of the ingoing primary particles (Figure 4, the thin dashed line in the right panel) is a major emission process. In soft X-ray bands, the synchrotron emissions for both ingoing and outgoing particles, and of both primary and the secondary particles all contribute to the calculated spectrum to explain RXTE observations, as Figure 4 shows. In optical bands, the synchrotron emissions for the secondary pairs (Figure 4, right) explain the observations.

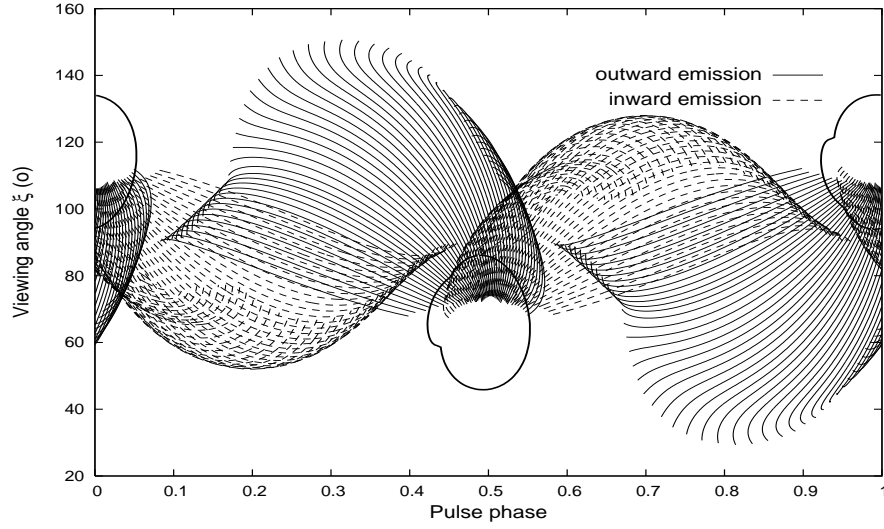


Figure 5. Emission region projected onto $(\phi; \xi)$ -plane for the magnetic surface, which has a polar angle of $\theta_p(\phi) = 0.95 \theta_1(\phi)$ on the stellar surface. An inclination angle is $\alpha = 65^\circ$ and the emission region extends from $r_{in} = 0.5r_n$ to $r = R_{1c}$, and extends around the rotation axis with the azimuthal angle of 180° . The solid lines and the dashed lines corresponding to the outward emissions and the inward emissions, respectively. The thick solid circles show the points of the radial distance $r = 0.05R_{1c}$ (section 3.1.4)

This energy dependency of the emission processes in the spectrum of the Vela pulsar is quite different from the emission mechanism of the Crab pulsar, of which the synchrotron self-inverse Compton process of the outgoing secondary pairs always dominates other emission processes (section 4.3). Unlike the double-peak pulse profile in whole energy bands of the Crab pulsar, therefore, we expect that the properties of the pulse profile, such as the peak position and number of the peaks in a single period, depend on the energy bands.

3.1.4 Pulse profile

In this section, we discuss the expected pulse profiles in γ -ray bands, in soft X-ray bands, and in optical/UV bands with a three-dimensional model. To adopt a more consistent three-dimensional geometry of the emission region, we use the solved two-dimensional gap structure (Figure 1, the left panel) presented in previous sections. As Figure 1 shows, the inner boundary of the outer gap is located at the radial distance $r_{in} = 0.5r_n$, where r_n is the radial distance to the inner boundary, and is $0.1R_{1c}$. Then, we assume the three-dimensional gap structure that the inner boundary on every field line, which penetrates the outer gap, is located at the position satisfied the radial distance $r_{in}(\phi) = 0.5r_n(\phi)$. Because the radial distance to the null charge surface varies with the azimuth ϕ , the radial distance to the inner boundary also varies with the azimuth. The lower boundary of the three-dimensional gap is defined by the surface of the last open field lines. For the upper boundary, we assume the

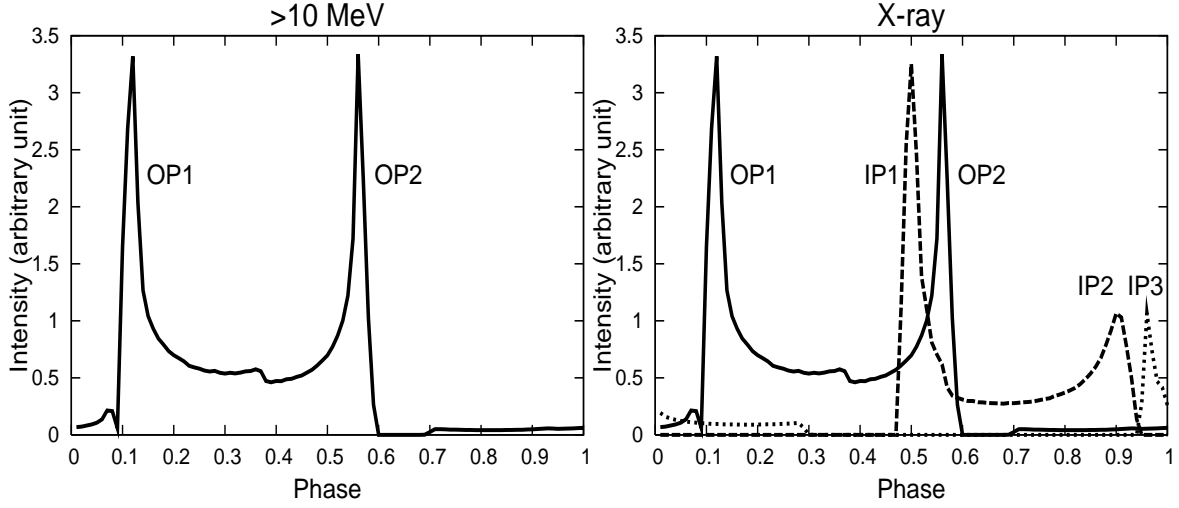


Figure 6. Pulse profile for the Vela pulsar. Left; Expected pulse profile in γ -ray bands by the outward emissions. Right; Expected pulse profile in X-ray bands. The solid line represents the pulse profile by the outward emissions. The dashed and the dotted line show the pulse profiles by the inward emissions of outside and inside of the null charge surface, respectively.

magnetic surface, of which the polar angle θ_p on the polar cap is $\theta_p(\phi) = 0.9\theta_1(\phi)$, where θ_1 is the polar angle of the last ϕ -open field lines. We assume that the outer gap expands around the rotational axis with the azimuthal angle of 180° . We note that in this paper we discuss the peak positions, which do not depend the emissivity distribution very well, in the pulse profile by ignoring the distribution of the emissivity. Although we need a more detailed model, which deals the three-dimensional distribution of electric field and of emissivity, to discuss the phase-resolved spectra with the pulse profile, the study of the phase-resolved spectrum is beyond the scope of this work.

We can anticipate that the emission direction in the observer frame is coincide with the particle motion. For example, the particle motion along the field lines in the north hemisphere, is described by $\mathbf{v} = \pm v_b \mathbf{b} + v_{\infty} \mathbf{e}$, where the plus (or minus) sign represents the outgoing (or ingoing) particles, v_0 is the velocity along the magnetic field line and is determined by the condition $|\mathbf{v}| = c$, \mathbf{b} is the unit vector of the magnetic field, for which we adopt a rotating dipole field in the observer frame, v_{∞} is the co-rotating velocity, and \mathbf{e} is the unit vector of the azimuthal direction. To compute the pulse profile, the emission direction, $\mathbf{n} = \mathbf{v}/c$, is interpreted in terms of the viewing angle $\theta = \theta_2$ and the pulse phase $\phi = \phi_e - \theta_e \sin \theta_e R/c$, where ϕ_e and r_e is the azimuthal direction of and the radial distance to the emission point, respectively. Figure 5 shows the emission regions projected onto $(\theta; \phi)$ -plane, where we adopt an inclination angle of $\theta = 65^\circ$. We choose the magnetic surface, of which the polar angle of the footpoint on the stellar surface is given as $\theta(\phi) = 0.95\theta_1(\phi)$.

The solid lines in Figure 5 are corresponding to the outward emissions, and the dashed lines are corresponding to the inward emissions. We can expect that the inward emissions also make peaks in the pulse profile; for example, the peaks due to the inward emissions appear around 0.5 phase and 0.9 phase for the observer with the viewing angle of 100° .

We discuss the expected pulse profile for each energy band. According to Figure 4, only outward curvature emissions contribute to the spectrum above 10 MeV. To calculate the pulse profile in γ -ray bands, therefore, we take into account the only outward emissions, which take place from the inner boundary to the light cylinder. Figure 6 (the left panel) shows the expected pulse profile in γ -ray bands with the viewing angle 97° . Because only outward emissions contribute to the emissions, we obtain double peak pulse profile, as previous studies have proposed (Romani & Yadigaroglu 1995; Romani 1996).

Unlike above 10 MeV, both outgoing and ingoing particles contribute to the spectrum of around 1 keV with the synchrotron emissions as Figure 4 shows. The right panel of Figure 6 shows the pulse profile, which includes both outward and inward emissions. For the inward emissions, we restricted the radial distance of the emission region with $r_s < r \leq 3r_n$, where the upper boundary $3r_n$ comes from the results of the dynamic model, in which very few ingoing pairs are produced beyond the radial distance $r > 3r_n$. We expected that the pulse positions of the outward synchrotron emissions are aligned with the phase of the peak above 10 MeV (OP1 and OP2 in Figure 6). The dashed line and the dotted line represent the pulse positions of the inward emissions beyond and below the null charge surface, respectively. As the dashed line shows, the inward emissions beyond the null charge surface make another two peaks, which are denoted with IP1 and IP2 in the figure, and the inward emissions below the null charge surface make one peak, which is denoted with IP3. Therefore, the present model predicts a multi-peak structure of the pulse profile in X-ray bands for the Vela pulsar.

We compare the expected peak phases in X-ray bands with the observed peak phases by RXTE (Harding et al. 2002), which indicates five peaks in a single period. In RXTE observations, the phase of the two peaks, which are denoted Pk1 and Pk2-soft in Figure 1 in Harding et al. (2002), are aligned with the phases of the two peaks in the γ -ray bands. With the present model, these two components of RXTE are explained by the synchrotron radiation of the outgoing particles, which produce two peaks (OP1 and OP2) relating with the γ -ray pulse profiles. The observed other two peaks, which are denoted Pk2-hard and Pk3 in Figure 1 in Harding et al. (2002), are corresponding to the model peaks denoted with IP1 and IP2, which come from the synchrotron emissions of the ingoing particles beyond the

null surface. Remarkably, the present model produces the observed phase separation (~ 0.4) of the two peaks.

RXTE Pk4 in Harding et al. (2002) will be explained by the inward synchrotron emissions below the null charge surface, which creates a peak (denoted with IP3) in Figure 6. RXTE observations show that the phase of Pk4 is aligned with the phase of the radio pulse. The present model also expect that the phase of the IP3 is close to the phase of the radio peak. Polarization studies for the observed radio emissions from the young pulsars indicate that the emission height of the emission is between 1 and 10 per cent of the light cylinder radius (Johnston & Westberg 2006). For the inclination angle $\alpha = 65^\circ$, because the radial distance to the null charge surface on the last opened lines in the meridional plane is about 10 per cent of the light cylinder, the radio emission region will be located near or below null charge surface for the Vela pulsar. For example, if the radio emissions are occurred at the radial distance that 5 per cent of the light radius, the radio pulse will be observed at the pulse phase of ~ 1 for the observer with the viewing angle $\beta = 97^\circ$, as the thick solid circles in Figure 5 show. Therefore, there is a possibility that we observe the pulse peak (IP3) from the inward emissions below the null charge at the phase aligned the phase of the radio peak. Although the predicted phase separation between IP2 and IP3 is smaller than the observed phase separation of RXTE Pk3 and Pk4, it may be because the real magnetic field structure around the neutron star will not be exactly described by the rotating dipole field, which was assumed in the present paper.

The pulse peaks, whose phases are in phase with the two-peaks in X-ray band (RXTE Pk1 and Pk2-soft in Harding et al. 2005) and in γ -ray bands (OP1 and OP2 in Figure 6), disappear in optical/UV bands (Romani et al. 2005). Furthermore, a new peak in optical/UV bands is observed at the phase between the phases of OP1 and of OP2 of Figure 6. We argue that the two peaks related with the higher energy emissions disappear because the primary particles do not contribute to the emissions in optical/UV bands, as Figure 6 (left) shows. The emissions from the secondary pairs take place at higher altitude than the altitude of the primary emission regions. In such a case, the phases of the pulse peaks of the outgoing secondary pairs is shifted inside the phases of the peaks produced by the outgoing primary particles. This may be reason for the shift of the observed first peak in optical/UV bands.

In summary of this section, we have calculated the phase averaged spectrum of the Vela pulsar with the two-dimensional electrodynamic outer gap model, and we have explained the observations in optical to γ -ray bands. We found that both emissions from the outgoing and

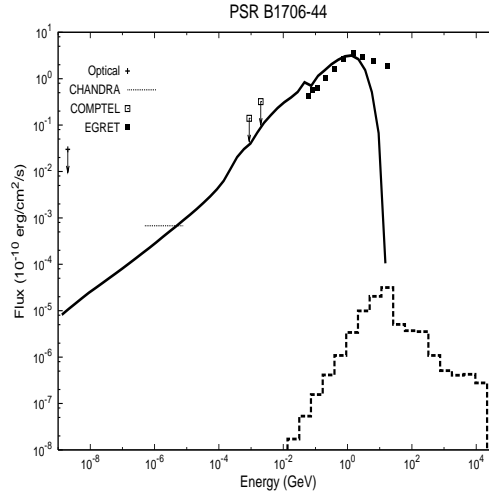


Figure 7. The spectrum of PSR B1706-44. The solid line shows the spectrum of the total emissions, which include the synchrotron and the curvature radiations from the outgoing and ingoing particles. The dashed line shows the spectrum of the inverse-Compton process of the primary particles. The observation data are taken from Chakrabarty & Kaspi (1998) for optical, Gotthelf et al. (2002) for CHANDRA, Carriera et al. (1995) for COMPTEL and Thompson et al. (1996) for EGRET.

ingoing particles are required to explain the observed spectrum. The present model predicts that the curvature radiation of the outgoing primary particles is the major emission process above 10 MeV, the outward and inward synchrotron emissions for the primary and secondary particles contribute to the emissions in X-ray bands, and the synchrotron radiation of the secondary particles explains the optical/UV emissions. We also calculated the pulse profile with a three-dimensional outer-gap model. The present model predicts the multi-peak pulse profile of RXTE observations with the outward and inward emissions.

3.2 PSR B1706-44

In this section, we apply the model to PSR B1706-44. PSR B1706-44 is the twin of the Vela pulsar. The magnetic field strength on the stellar surface and the spin down age of the PSR B1706-44 are similar to the Vela pulsar. However, the spectral behavior above the spectral energy peaks observed by the EGRET are different. The EGRET spectrum of the PSR B1706-44 extends above 10 GeV bands from the energy peak, 1 GeV, with a larger spectral index than that of the Vela pulsar. In the X-ray bands, although CHANDRA and XMM-Newton observations have detected the non-thermal emissions, the emission mechanism has not been discussed in detail. Because the inclination angle is not constrained well for this pulsar, we adopt an inclination angle of $\theta = 65^\circ$ of the Vela pulsar. For the surface X-ray emissions, we apply the temperature $kT_s = 0.14$ with the effective radius $R_{\text{eff}} = 4 (d=2.5 \text{ kpc})^2 \text{ km}$ (Gotthelf et al. 2002).

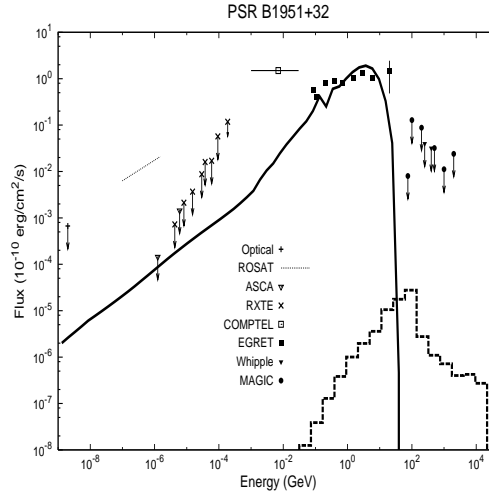


Figure 8. The spectrum of PSR B1951+32. The solid line shows the spectrum of the total emissions, which include the synchrotron and the curvature radiations from the outgoing and ingoing particles. The dashed line shows the spectrum of the inverse-Compton process of the primary particles. The observation data are taken from Kulkarni (1988) for optical, Sarabhai et al. (1995) for ROSAT, Chang & Guo (2000) for ASCA and RXTE, Kuiper et al. (1998) for COMPTEL, Ramakrishna et al. (1995) for EGRET, and Albert et al. (2007) for Whipple and MAGIC.

Figure 7 shows the spectrum of the total emissions, which include the emissions for the primary and the secondary particles. The solid line shows the spectrum of the synchrotron and curvature radiation, and the dashed line represents the spectrum of the inverse-Compton process. As the solid line shows, the calculated X-ray emissions explain the flux of CHANDRA observations but the predicted spectral index is ~ 0.5 , which is defined by $I \propto E^{-\alpha}$, does not explain the index ~ 1 of CHANDRA observation. However, the present model is consistent with XMM-Newton observation of PSR B1706-44, which indicates the spectral index of ~ 0.5 (McGowan et al. 2004).

In γ -ray bands, the predicted spectrum explains the EGRET observations below 1 GeV very well. However, the observed spectral slope above 1 GeV is not explained by the present model, which predicts the exponential decrease of the flux beyond the spectral peak energy. The observed harder spectral index beyond the spectral peak energy may be related with the three-dimensional effect which due to that the line of sight of the observer passes the outer gap. Also, because EGRET observed the photons around 10 GeV bands with a less sensitivity, it is important to observe the γ -ray emissions around 10 GeV with a better sensitivity. It will be done by GLAST.

3.3 P SR 1951+ 32

P SR B1951+ 32 is one of the older γ -ray pulsars with the spin down age, 1.1×10^5 yr, and has a stellar magnetic field of $B_s = 9.7 \times 10^1$ Gauss. The property of the X-ray emissions of B1951+ 32 is not constrained observationally, because the X-ray and soft γ -ray emissions is so weak. For example, the X-ray emission property determined by ROSAT observations (Saharab et al. 1995) conflicts with the upper limits determined by the RXTE and ASCA observations (Chang & Ho 1997; Chang & Guo 2000). We apply the theory to P SR B1951+ 32 to show the predicted spectrum from optical through γ -ray bands with the present model.

We infer the surface X-ray emissions of P SR B1951+ 32 from the values of the Geminga pulsar, which is a γ -ray pulsar with a similar spin down age, 3×10^5 yr, with P SR B1951+ 32. For the Geminga pulsar, the surface temperature is $kT_s = 0.043$ keV with an effective area $R_{\text{eff}} = 13$ ($d=0.12$ kpc)² (Kargaltsev et al. 2005), which means that the observed thermal emissions are most likely emitted from the bulk of the neutron star surface. For P SR B1951+ 32, therefore, we adopt the surface temperature $kT_s = 0.043$ keV with an effective radius $R_{\text{eff}} = 13$ ($d=2.5$ kpc)². We use an inclination angle of $\theta = 65^\circ$.

Figure 8 shows the calculated spectrum of the total emissions, which include the emissions for the primary and the secondary particles. The solid line is the spectrum of the synchrotron and the curvature radiation, and the dashed line shows the spectrum of the inverse-Compton process. As the solid line shows, the present model predicts that the X-ray and soft γ -ray emissions are so weak to detect with the present instruments, and the result does not explain the fluxes determined by ROSAT and COMPTEL. On the other hand, the present result is consistent with the upper limits determined by the RXTE and ASCA observations. Above 100 MeV, the model spectrum explains the EGRET observations, and is consistent with the upper limits determined by Whipple and MAGIC observations.

4 DISCUSSION

4.1 Phase resolved-spectrum

With the RXTE observations, Harding et al. (2002) proposed the spectral index s , which is defined by $I \propto E^{-s}$, of $s = 1$ for the phase-resolved spectrum of the peak (Pk 2-soft in figure 1 of Harding et al. 2002), which appears between the two peaks, whose phases are aligned with the peak positions in γ -ray bands. As we discussed in section 3.1.4, the present model explains emission mechanism of RXTE Pk 2-soft with the synchrotron emissions of

the ingoing particles, which create a peak (Figure 6, IP1) in the pulse profile. Although the spectrum in Figure 4 is calculated using two-dimensional model, we may be able to read the spectral index of the phase-resolved spectra of the peak IP1 from Figure 4 (from the slope of the thin dashed-dotted line in the right panel), which predicts the spectral index $s \approx 0$ for the IP1 emissions. For the reason of this discrepancy between the spectral indexes of RXTE and the present model, we argue that the three-dimensional structure affects the phase-resolved spectrum, and/or that RXTE observations might not determine the spectral behavior in the X-ray bands very well due to a bright synchrotron X-ray nebula. The present model predicts the inward synchrotron emissions for the ingoing primary particles (Figure 4, the thin dashed line in the left panel) contribute to the spectrum in hard X-ray and soft γ -ray bands. Therefore it is important to measure the phase-resolved spectra and the pulse profiles of the Vela pulsar in the hard X-ray and soft γ -ray bands to see how the phase-resolved spectra and the pulse profiles evolve.

4.2 Correlation between radio emission and the outer gap emission

Recently, the correlation between the arrival time of the radio emissions and the shape of the non-thermal X-ray pulse profile of the Vela pulsar was discovered (Lommen et al. 2007). Although the radio emission mechanism has not been understood well, the polarization measurement indicates a correlation between the magnetic field geometry of the polar cap region and the swing of the position angle of the polarization of the radio emissions. Therefore, the polar cap accelerator model as the origin of the radio emissions from the pulsar has been widely accepted. A magnetospheric model having both the polar cap accelerator and the outer gap accelerator has been proposed upon request to balance between the energy loss rate and the angular momentum loss rate, which is equal to the energy loss rate divided by the angular velocity of the star, of the global magnetosphere (Shibata 1991; 1995). Although the polar cap accelerator and the outer gap accelerator can not exist on the same magnetic field lines because of the different current directions in the polar cap and outer gap accelerators, the polar cap accelerator affects the outer gap accelerator to obtain the torque balance. According to this model, therefore, even though the non-thermal X-rays originate from the outer gap accelerator, some correlations between X-ray emissions and the radio emission are expected. Furthermore, the present model also predicts that the outer gap accelerator affects the polar cap accelerator with the inward emissions, which pass near the

stellar surface. The inward emissions will affect the circumstance around polar cap region through the pair-creation process and/or the scattering process.

4.3 Inward emissions from the Crab pulsar

Unlike the Vela pulsar, the Crab pulsar has only two peaks in the pulse profile in optical through γ -ray bands. This indicates that the observed emissions of the Crab pulsar are dominated by the outward emissions in whole energy bands. For the Crab pulsar, the photons above 1 GeV emitted via the curvature radiation in the outer gap are converted into the pairs outside the gap by the pair-creation process by the magnetospheric X-ray photons emitted by the secondary pairs. Outer gap model predicts the synchrotron and the inverse-Compton processes of the secondary pairs explain the observed emissions in optical through γ -ray bands. As we discussed in section 3.1.3 (Figure 4, right), the outward synchrotron radiation by the outgoing secondary pairs created by the magnetospheric X-rays is much brighter than the inward synchrotron radiation, because the outgoing γ -rays emitted by the curvature radiation is much more than the ingoing γ -rays. For the Crab pulsar, therefore, we can expect that the outgoing secondary pairs produce the observed spectrum with the synchrotron and the inverse-Compton process. Because the flux of the outward emissions of the secondary particles is much (say one or two order) larger than that of the inward emissions, the pulse profiles have strong two peaks in a single period in optical through γ -ray bands for the Crab pulsar. Although we expect contribution of the inward emissions at ϕ -pulse phase, it must be difficult to separate the tiny flux of the inward emissions from ϕ -pulse outward emissions inside null charge surface and/or from the strong background emissions from the synchrotron nebula.

ACKNOWLEDGMENTS

The authors appreciate fruitful discussion with K.S. Cheng, K. Hirotani and R. Taam. This work was supported by the Theoretical Institute for Advanced Research in Astrophysics (T-IARA) operated under Academia Sinica and National Science Council Excellence Projects program in Taiwan administered through grant number NSC 96-2752-M-007-001-PAE.

REFERENCES

Albert J. et al., 2007, *ApJ*, 669, 1143

- Carramiñana A. et al., 1995, *A & A*, 304, 258
- Chakrabarty D. & Kaspi V M., 1998, *ApJL*, 498, 37
- Chang H.-K. & Ho C., 1997, *ApJL*, 479, 125
- Chang H.-K. & Guo T.-F., 2000, *Pulsar Astronomy – 2000 and Beyond*, *ASP Conference Series*, 202, 327
- Chang H.-K., Boggs S., Chang Y.-H. for the NCT collaboration, 2007, *AdSpR*, 40, 1281
- Cheng K. S., Ho C. & Ruderman M. 1986a, *ApJ*, 300, 500
- Cheng K. S., Ho C. & Ruderman M. 1986b, *ApJ*, 300, 522
- Cheng K. S., & Zhang L. 1996, *ApJ*, 463, 271
- Cheng K. S., Ruderman M. & Zhang L. 2000, *ApJ*, 537, 964
- Fierro J M., Michelson P F., Nolan P L. & Thompson D J., 1998, *ApJ*, 494, 734
- Goldreich P. & Julian W. H. 1969, *ApJ*, 157, 869
- Gotthelf E. V., Halpern J P. & Dodson R., 2002, *ApJL* 567, 125
- Harding A K., Strickman M. S., Gwinn C., Dodson R., Mo et D. & McCulloch P., 2002, *ApJ*, 576, 376
- Harding A K., Usov V. V., Muslimov A. G., 2005, *ApJ*, 622, 531
- Hirota N. K., 2006, *ApJ*, 652, 1475
- Hirota N. K., 2007, *ApJ*, 662, 1173
- Jia J. J., Tang, Anisia P. S., Takata J., Chang H.-K. & Cheng K. S., 2007, *AdSpR*, 40, 1425
- Kamae T., et al. 2007, *astro-ph/0709.1278*
- Kanbach G., Slowikowska A., Kellner S. & Steinle H., 2005, *AIP Conference Proceedings*, 801, 306
- Kargaltsev O. Y., Pavlov G. G., Zavlin V. E. & Romani R. W., 2005, *ApJ*, 625, 307
- Konopelko A. et al., 2005, *Proceedings of the 29th International Cosmic Ray Conference*, Pune, India, 4, 139
- Krishnamohan S. & Downs G. S., 1983, *ApJ*, 265, 372
- Kuiper L., Hermesen W., Bennett K., Carramiñana A., Lyne A., McConnell M. & Schoenfelder V., 1998, *A & A*, 337, 421
- Kulkarni S. R., Clifton T. C., Backer D. C., Foster R. S. & Fruchter A. S., 1988, *Natur*, 331, 50
- Lommen, A. et al., 2007, *ApJL*, 657, 436
- Manzali A., De Luca A., Caraveo P. A., 2007, *ApJ*, 669, 570
- McGowan K. E., Zane S., Cropper M., Kennea J. A., Cordova F. A., Ho C., Sasseen T. &

- Vestrand W. T. , 2004, *ApJ*, 600, 343
- Mestel L. , 1999, *Stellar Magnetism*, International Series of Monographs of Physics. Oxford Univ. Press, Oxford
- Mignani R. P. , Bagnulo S. , Dyks J. , Lo Curto G. & Slowikowska A. , 2007, *A & A*, 467, 1157
- Muslimov A. G. & Harding A. K. .2003, *ApJ*, 588, 430
- Muslimov A. G. & Harding A. K. .2004, *ApJ*, 606, 1143
- Ram anam urthy P. V. et al., 1995, *ApJL*, 447, 109
- Romani R. W. & Yadigaroglu I. A. .1995, *ApJ*, 438, 314
- Romani R. W. .1996, *ApJ*, 470, 469
- Romani R. W. , Kargaltsev, O. & Pavlov, G. G. , 2005, *ApJ*, 627, 383
- Ruderman M. A. & Sutherland P. G. , 1975, *ApJ*, 196, 51
- Sa -Harb S, Ogelman H & Finley J. P. , 1995, *ApJ*, 439, 722
- Shibanov Yu A. , Koptsevich A. B. , Sollem an J & Lundqvist P. , 2003, *A & A*, 406, 645
- Shibata S., 1991, *ApJ*, 378, 239
- Shibata S., 1995, *MNRAS*, 276, 537
- Strickman et al., 1996, *ApJ*, 460, 735
- Sturrock P. A. , 1971, *ApJ*, 164, 529
- Tang P. S. Anisia, Takata J., Jia, J. J., Cheng K. S., 2008, *ApJ*, in press
- Takata J., Shibata S. & Hirotsu K. .2004, *MNRAS*, 354, 1120
- Takata J., Shibata S., Hirotsu K. & Chang H.-K. .2006, *MNRAS*, 366, 1310
- Takata J., Chang H.-K. & Cheng K. S., 2007 *ApJ*, 656, 1044
- Takata J. & Chang H.-K. , 2007 *ApJ*, 670, 677
- Thompson D. J. et al., 1996, *ApJ*, 465, 385
- Thompson D. J., 2004, in *Cosmic Gamma Ray Sources*, ed. K. S. Cheng & G. E. Romero (Dordrecht: Kluwer), 149